Materials & Design 242 (2024) 113013

Contents lists available at ScienceDirect

Materials & Design

journal homepage: www.elsevier.com/locate/matdes

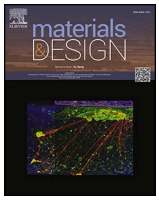

Tribological behavior and biocompatibility of novel Nickel-Free stainless steel manufactured via laser powder bed fusion for biomedical applications

Chinmayee Nayak [a,1,*], Abhinav Anand [a,1], Nikhil Kamboj [a], Tuomas Kantonen [a], Karoliina Kajander [b], Vilma Tupala [b], Terhi J. Heino [b], Rahul Cherukuri [c], Gaurav Mohanty [c], Jan Čapek [d], Efthymios Polatidis [e], Sneha Goel [a,f], Antti Salminen [a], Ashish Ganvir [a]

[a] Research group of Digital Manufacturing and Surface Engineering, Department of Mechanical and Materials Engineering, University of Turku, FI-20500 Turku, Finland
[b] Institute of Biomedicine, Faculty of Medicine, University of Turku, Finland
[c] Materials Science and Environmental Engineering, Tampere University, 33014 Tampere, Finland
[d] Applied Materials Group, Laboratory for Neutron Scattering and Imaging, Paul Scherrer Institute, Switzerland
[e] Laboratory of Technology and Strength of Materials, Department of Mechanical Engineering and Aeronautics, University of Patras, 26500 Rion, Greece
[f] Advanced materials for nuclear energy, VTT Technical Research Centre of Finland, Finland

ARTICLE INFO

Keywords:
Nickel-Free Stainless Steel
Additive Manufacturing
Laser Powder Bed Fusion
Tribology
Biocompatibility
Biomedical Engineering

ABSTRACT

Due to the risk of releasing carcinogenic nickel ions from conventional 316L stainless steel under a corrosive human body environment, a new variant of steel termed nickel-free stainless steel (NiFSS) has been investigated. The present study investigates the tribological properties and biocompatibility of NiFSS manufactured via laser powder bed fusion (PBF-LB/M). The ferritic NiFSS exhibited significantly lower coefficient of friction (0.08 to 0.28) and wear rate (1.60×10^{-6} mm^3/Nm to 6.60×10^{-6} mm^3/Nm) compared to reported values for austenitic 316L SS, under both dry and simulated body fluid (SBF) conditions and various sliding geometries. This improvement is attributed to the superior hardness (3.394 ± 0.1340 GPa) and elastic modulus (238 ± 9.0797 GPa) of NiFSS. To assess the biocompatibility, the viability of mouse pre-osteoblastic MC3T3-E1 cells was evaluated with an Alamar Blue assay when the cells were cultured on top of PBF-LB/M built NiFSS and 316L SS samples. The results indicated that even though cell growth was most optimal on regular cell culture plastic, cell viability was better maintained on PBF-LB/M built NiFSS compared to 316L SS. Therefore, the results of the present study propose that PBF-LB/M fabricated NiFSS holds promise for application in biomedical devices for joint arthroplasty.

1. Introduction

Stainless steels (SS) are favored for biomedical implants because of their excellent malleability, robust mechanical properties, resistance to corrosion, and biocompatibility. Among several varieties of SS, AISI 316L SS (316L SS) has become notably popular in the biomedical sector, especially in joint replacement surgeries, due to its cost-effectiveness and reliability, supported by extensive testing data on its mechanical strength, corrosion resistance, and biocompatibility [1]. However, the after-effects of prolonged usage of 316 L implants in the human body environment have been debated in the scientific community. Studies have shown that 316 L implants can corrode and release toxic nickel ions in the bloodstream, which has been reported to be carcinogenic for rats [2]. Over time, in the human tissue and interstitial fluid environments, which include various ions, such as chloride, amino acids, and proteins, 316L SS has demonstrated undesirable instances of pitting and crevice corrosion [3]. Any possible release of nickel ions from 316L SS in critical concentrations inside the human body can cause allergic reactions [4]. Furthermore, nickel compounds have been labeled carcinogenic to humans by the International Agency for Research on Cancer (IARC) [5]. Due to advancements with time and low success rates with 316L SS, it has become almost obsolete and is being replaced by newer materials. Therefore, in efforts to manufacture biomedical implants with enhanced safety and reduced risk of nickel ion release, researchers at ETH Zurich developed a novel type of steel, named as P558 grade by substituting nickel with an increased concentration of manganese and incorporating

* Corresponding author.
E-mail address: chinmayee.nayak@utu.fi (C. Nayak).
[1] Equally contributed as first author.

https://doi.org/10.1016/j.matdes.2024.113013
Received 10 April 2024; Received in revised form 6 May 2024; Accepted 8 May 2024
Available online 9 May 2024

nitrogen as an additional alloying element [6]. Nitrogen possesses a similar capability to stabilize the austenitic structure as nickel, while also enhancing the corrosion resistance of steel. Thomann *et al.* [4] developed a new alloy named P558 grade, which increased manganese, molybdenum, and nitrogen and replaced Nickel. Further, Fini et al. [7] conducted an in-vivo and in-vitro investigation on P558 grade to evaluate its biocompatibility and osteointegration capabilities. Their findings demonstrate that P558 exhibits favorable biocompatibility both in laboratory settings (in vitro) and within living organisms (in vivo). Moreover, compared to other materials tested (Ti6Al4V and ISO 5832–9 SS), P558 enhanced the processes of osteointegration, indicating its potential as a promising biomaterial for various biomedical applications. There has been a development of austenitic stainless steels with elevated nitrogen and molybdenum levels, alongside reduced carbon and nickel content, specifically for biomedical applications [8]. The tradename of PANACEA stands for protection against nickel allergy, corrosion, erosion, and abrasion and is the most commonly used nickel-free stainless steel (NiFSS) for biomedical applications.

Biomedical implants are patient-specific, and customized designs are required. Conventional manufacturing methods lack the accuracy for complex designs and personalized features crucial in biomedical implants. Additive manufacturing (AM), also known as 3D printing, is a technique that builds three-dimensional objects layer-by-layer based on CAD models [9]. This manufacturing method, widely used in rapid prototyping and customized designs, provides flexibility and accuracy in manufacturing, eliminating the requirement for tooling. As a result, it simplifies the fabrication process and reduces associated expenses [10]. Additive manufacturing of metals, such as laser powder bed fusion (PBF-LB/M), offers design flexibility, intricate geometries with capabilities of manufacturing of fine porous structures like specialized scaffolds, and tailored solutions for biomedical implants with potential cost efficiencies through reduced material waste and manufacturing time [11]. Several investigations have explored the mechanical, tribological, and corrosion properties of 316L SS implants, manufactured through PBF-LB/M, in simulated body-fluid (SBF) environments [12–16]. The selective laser melting (SLM-450) built 316L SS showed 80 % higher cell viability rate than its wrought counterpart (72 %) due to the better blocking of harmful ions release from SLM-450 built 316L SS to the environment [17]. However, only one previous study has documented the production of NiFSS samples using PBF-LB/M and that too from the same authors group [18].

The restrictions and shortcomings presented by the cumbersome multi-step conventional techniques have led to escalated research on AM techniques for the manufacturing of biomedical implants [19]. Nowadays, PBF-LB/M has not only emerged as a competent solution for the fabrication of the biomedical implants or scaffolds for bone tissue engineering (BTE) owing to the complex design and accuracy in manufacturing but also used as a modern technique facilitating different modes of functionalization of biomedical implants to manufacture drug delivery systems (DDSs) [20]. Furthermore, PBF-LB/M offers other advantages, such as absence of post-processing stages and capability to manufacture biomedical products with wider window of pore sizes in range of 100–1000 μm when compared to the other metal AM techniques. However, the downside of using PBF-LB/M are keyhole porosity, cracking, lack of fusion which can ultimately hamper the functional performance of the fabricated part [21].

Evaluating the tribological properties, such as wear rate, coefficient of friction, and lubrication of biomedical implants manufactured via PBF-LB/M is essential to guarantee the durability and effectiveness of such implants, especially in biomedical applications susceptible to failures associated with friction and wear, such as artificial joints and implants [22,23]. Friction is one of the main problems leading to materials being serviced; therefore, it is also important to investigate the wear resistance of NiFSS. Wear, or the amount of material removed, is roughly proportional to the contact load and sliding distance and usually inversely proportional to the hardness [24]. Thomann *et al.* [4] have indicated that the PANACEA P558 alloy, a high-nitrogen NiFSS, shows enhanced wear resistance compared to 316L SS when produced through the conventional casting process in an electric arc furnace. Zhao *et al.* [24] investigated the effect of cold deformation on friction in nickel free high-nitrogen stainless steels (NFHNSSs) produced by forging in distilled water and SBF solution. The results suggested that NiFSS demonstrates impressive work-hardening capabilities, with the dry-wear rate initially declining before increasing as cold deformation rises. The coefficient of friction (CoF) depends on several parameters such as geometry, normal load, lubrication, sliding speed, relative surface motion, the surface roughness of the rubbing surfaces, system rigidity, temperature, stick–slip, relative humidity, type of material and vibration [25–28].

As discussed above, the adverse effects of nickel ions on human physiology have led to the development of NiFSS. They appear to be less cytotoxic compared to conventional stainless steel AISI 316L, which is often applied e.g. in orthopedic instruments and implants. Ren et al. [29] utilized a platelet-rich plasma adhesion test and showed that NiFSS (BIOSSN4) had better blood compatibility than 316L stainless steel. However, there are no previous studies on the biocompatibility of NiFSS fabricated via PBF-LB/M.

The novelty of the present work lies in the manufacturing, tribological and biological assessment of NiFSS using the PBF-LB/M method. Following the manufacturing of NiFSS, its mechanical properties were assessed through the nanoindentation technique. While numerous studies have explored the tribological properties of conventionally produced NiFSS, no study has so far reported the tribological properties and biocompatibility of NiFSS samples, manufactured by PBF-LB/M, in both dry and SBF conditions. Hence, this study aimed to investigate the tribological properties, including CoF and wear rate, of PBF-LB/M built NiFSS when subjected to a zirconia ball as a counter body. The present study employed two reciprocating geometries (linear and eight/butterfly) under both dry and lubricated conditions using SBF. The experiments were conducted at a constant normal load and sliding speed using an automated Bio-Tribometer, allowing for the evaluation of the effect of geometry and lubrication on coefficient of friction and wear rates under various movements representative of practical implant applications. Additionally, the biocompatibility of the PBF-LB/M built NiFSS was also investigated by utilizing a well-established osteoblast-like cell line.

2. Materials and methods

2.1. Sample preparation

Gas atomized NiFSS powder was supplied by Sandvik Osprey Ltd [30]. The powder composition of the batch is shown in Fig. 1. As compared to austenitic stainless steel like AISI 316L, in this case, nickel (Ni) has been replaced by a higher amount of manganese (Mn) along with the addition of nitrogen (N) in the composition to stabilize the austenitic phase, whereas chromium (Cr) and molybdenum (Mo) stabilized the ferrite phase. As per Schaeffler and Delong calculations [31], the chromium equivalent (Cr_{eq} = [Cr] + 1.4[o] + 1.5[Si] + 0.5[Nb]) in this steel is 22.89 % whereas nickel equivalent (Ni_{eq} = [Ni] + 30×([C] + [N]) + 0.5[Mn]) is 9.64 %. Fig. 2, nickel-free steel is anticipated to consist of duplex steel containing both austenite and ferrite phases.

Scanning electron microscopy (SEM) was performed to analyze the powder morphology using Thermo Scientific Apreo 2. The powder particles were observed to be spherical and had some protuberances as shown in Fig. 3**(a)**. Further, powder size distribution was analyzed using Malvern MS3000. The D10, D50, and D90 values were 17.9 μm, 28 μm, and 44.6 μm, respectively.

In this work, to manufacture the NiFSS samples via PBF-LB/M, Aconity MIDI + machine was used. System has one SM Fiber laser with maximum power of 400 W and a 3D-scanner. Since NiFSS is an unexplored material in metal AM, no databases were available for the process parameters like laser power, scanning speed, layer thickness,

Element →	Cr	Mn	Mo	Si	N	C	Co	S	P	Ni	O	Nb
wt. % →	17.300	11.400	3.240	0.700	0.177	0.028	0.010	0.005	0.017	0.100	0.156	0.010

Fe
balanced

Fig. 1. Chemical composition of Ni-free steel in weight %.

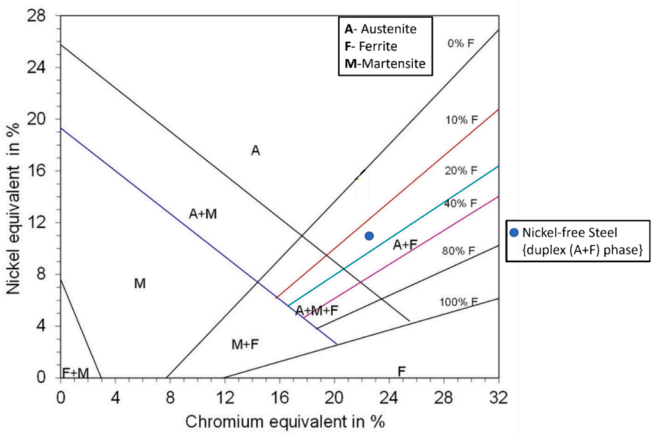

Fig. 2. Positioning of NiFSS within the Schaeffler diagram [32].

and hatch distance involved in the manufacturing. A design of experiment was adopted in which laser power was varied from 110 W to 300 W, the scanning velocity from 400 mm/s to 2000 mm/s, and hatch distance from 0.05 mm to 0.08 mm. Layer thickness of 30 μm and laser beam diameter on powder bed of 80 μm were kept constant throughout the experiments. A total of sixty samples were printed based on the above-mentioned parameters under an inert argon gas environment with an oxygen level below 500 ppm. The table (Table S1) in supplementary data containing the parameters used during optimization. The relative density of the samples was measured according to Archimedes' principle to find the optimal parameter values, i.e., samples were weighed in the open air and submerged in distilled water. The measurement was conducted three times for each sample. A relative density of 98.469 % was achieved with laser power 160 W, scanning speed 600 mm/s, and hatch distance 0.08 mm. The laser scanning strategy was unidirectional, with 70 degrees of rotation for each preceding layer.

2.2. Structural characterization

X-ray diffraction (XRD) was performed on powder and as-built samples for the phase identification using Malvern Panalytical Empyrean equipment with Cu-Kα radiation to record the data in a 2θ range of 30° to 90°. For microscopic analysis via Scanning Electron Microscope (SEM), the as-built samples were ground to a fine 4000-grit size using SiC papers and were further polished using colloidal silica suspension. Energy Dispersive Spectroscopy (EDS) was also performed to identify the elements present. EBSD samples were polished metallographically to the fine solution of 0.02 um colloidal silica suspension using a Struers Tegramin automatic polishing machine. A Zeiss ultra-plus field emission SEM, equipped with an Oxford instrument symmetry EBSD detector, was used for EBSD microstructure imaging. An acceleration voltage of 20 kV was used for EBSD imaging. An open-source MTEX toolbox [33] was used for the EBSD data analysis.

2.3. Hardness and elastic modulus

Nanoindentation tests were performed using an *Alemnis AG* (Switzerland) in-situ nanoindenter inside a Zeiss Leo Scanning Electron Microscope with a three-sided pyramidal Berkovich diamond indenter tip. An indentation grid of 10 x 10 was performed. The indentation profile comprised a linear profile with load-controlled mode with a load target of 150 mN, which is equivalent to 1.3 μm depth approximately. The tip area was calibrated on fused silica. Indent spacing of 15 μm was used to ensure an indentation spacing/indentation depth ratio is greater than or equal to 10 to prevent an overlap of the plastic zones between neighboring indents which was suggested by Phani *et.al* [34]. The resulting map of 100 indents covers an area of 150 μm x 150 μm on the sample. The obtained load–displacement data was analyzed using Oliver Pharr's method to measure hardness and modulus [35,36]. EBSD maps were taken before indentation to estimate the phase fractions, average grain sizes, and orientation information.

2.4. Tribology testing

An automated single station Bio-Tribometer (DUCOM, work order-2170) was utilized to analyze the tribological characteristics of the PBF-LB/M manufactured NiFSS cylindrical specimens with a diameter of 30 mm and a height of 15 mm. The present tribological investigation employed a ball-on-disc experimental setup (Fig. 4).

The variation in parameters including the length and perimeter, of different reciprocating geometries (linear and eight/butterfly), have been tabulated in Table 1. All the experiments were carried out at a fixed sliding speed of 10 mm/s and a sliding time of 90 min with a normal load of 60 N. The experiments were carried out under dry (at room temp) and SBF lubricated (at human body temp of 37 °C) conditions. The lubricant used was Simulated Body Fluid (SBF), prepared as Kokubo et al.

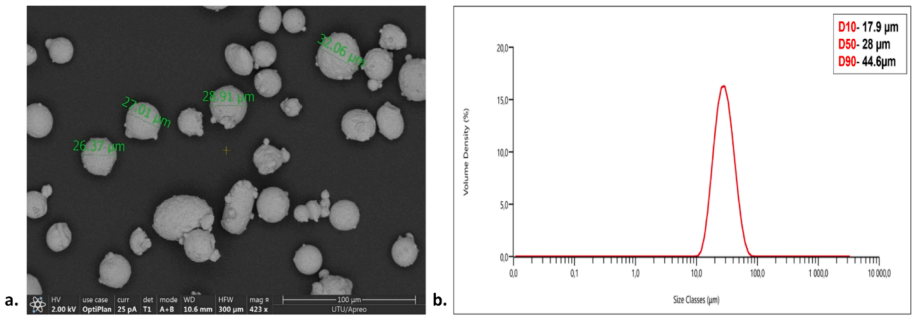

Fig. 3. (a) SEM image of Ni-free stainless steel (NiFSS) powder (b) Particle size distribution curve of NiFSS powder.

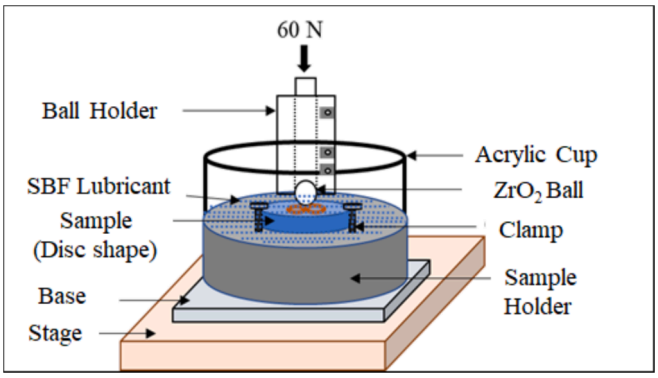

Fig. 4. Schematic view of a ball-on-disc bio-tribometer configuration.

Table 1
Variation of parameters for different reciprocating geometries.

Sliding Geometry	Linear	Eight
Sliding geometry Dimensions (mm)	4 (length)	15 (perimeter)
Sliding Speed (mm/s)	10	10
Total Sliding Distance (m)	20	37.5

instructed in [37]. An average of three tests were conducted for each condition and geometry to report the average values. Before the investigation, test samples were first polished up to 0.1 μm. A zirconia ball of 6 mm diameter, elastic modulus (E) 248.28 GPa, and Poisson's ratio (υ) 0.27 was used as the counter body against the test samples [38]. The coefficient of friction was continuously recorded using a load cell throughout the test to evaluate the effect of different reciprocating geometries. The wear volume was obtained through optical profilometry of the wear scars, which was done via Alicona Infinite FocusSL and subsequently utilized to calculate the wear rate of the samples using Archard's wear equation [39]. The scanning electron microscopy (SEM) analysis of wear scars revealed the wear mechanisms and the damage severity during the sliding wear test.

2.5. Assessment of biocompatibility

The biocompatibility and possible cytotoxicity of NiFSS and 316L SS fabricated via PBF-LB/M was evaluated by assessing the viability of mouse pre-osteoblastic cells (MC3T3-E1 clone 4, CRL-2593™) using the Alamar Blue assay (Invitrogen, DAL1100). Alamar Blue assay reagent undergoes colorimetric change in response to metabolic function in living cells, and the intensity of fluorescence produced is proportional to the number of cells. The cell growth medium consisted of phenol-red free αMEM (Gibco, 41061029), fetal bovine serum (FBS, 10 %, Gibco, 10270106) and Penicillin–Streptomycin (1 %, Gibco, 15140122).

Before the experiment, a standard curve was prepared to determine the specific correlation of Alamar Blue fluorescence to MC3T3-E1 cell number. For this, cells were seeded on a 24-well plate in a range of 0 to 125 000 cells/well in 1 ml culture medium. After 18 h of cell seeding, an Alamar Blue assay was performed according to the manufacturer's instructions and the fluorescence was measured with Ensight Multimode Plater Reader (Perkin Elmer) (excitation/emission 560/590 nm). Incubation time for Alamar Blue was 3 h. Fluorescence values were plotted against the number of plated cells to obtain a standard curve for cell growth.

For the cytotoxicity experiments, NiFSS and 316L SS samples fabricated via PBF-LB/M were sawn into smaller pieces with an average surface area of 41.8 mm^2 (±10.8 mm^2) for NiFSS and 30.5 mm^2 (±1.34 mm^2) for 316L SS and polished. Before use in cell culture, the samples were sterilized by dry heat (180 °C, 4 h), after which they were placed in 24-well cell culture plate. MC3T3-E1 cells were seeded on top of NiFSS or 316L SS samples (10,000 cells in 10 μl). After 2 h of cell attachment, 1 ml of growth medium was added to each well. Similarly, cells were also seeded on regular cell culture plastic without materials to serve as a positive control group. The cells were maintained at standard cell culture conditions of + 37 °C, 5 % CO_2. Medium was changed every 2–3 days. Cells viability was assessed on days 1, 3, 5, 7 and 10 of culture, and the fluorescence was measured as described above. The standard curve equation was used to calculate the number of cells in each group based on the fluorescence intensity. Each experiment included four technical repeats (i.e. individual samples) for NiFSS and two to three technical repeats for 316L SS and the whole experiment was repeated five times. For the third and fourth repeats, the samples from earlier repeats were cleaned with a cotton swab and sterilized again for reuse. Completely new samples were used for the fifth repeat. Statistical testing for normally distributed data was performed using ANOVA followed by Tukey's multiple comparisons test with GraphPad Prism (v10.0).

3. 3.Results and discussions

3.1. Basic characterization and phase analysis

As shown in Fig. 5(a) SEM micrographs of the as-built sample after polishing (b) EBSD phase mapping (red-BCC, green-FCC) (c) EDS for detecting elements in the scanned region (marked as rectangle region), SEM image revealed the presence of small pores in the fabricated sample, validating the finding that only 98.469 % relative density was achieved with the optimized process parameters. From the spectrum obtained from EDS mapping, a slight variation in element composition was observed as compared to powder, possibly due to the vaporization of alloying elements [40].

The EBSD phase map showed a fully ferritic phase highlighted by a red area in the as-built specimen, which is also confirmed by XRD, as shown in Fig. 6. Unlike the composition containing both ferrite and austenite phase (Fig. 2), NiFSS powder was fully ferritic as only bcc phase peaks were observed in the XRD pattern due to the high cooling rate of molten metal droplets during the gas atomization process, inhibiting the growth of austenite (fcc) phase. Similarly, no phase transformation was observed in the laser melting and solidification during PBF-LB/M. Small XRD peaks were observed at 2 theta angles of 54° and 77° because as-built sample was hot mounted in a bakelite resin. Calcium carbonate and silicon oxide present in bakelite contributed to these peaks. In PBF-LB/M, the molten metal can attain a temperature of approximately 3000 °C and experiences a rapid cooling at a rate of 10^6 to 10^8 °C/s during the solidification, which results in the retaining of high-temperature delta ferrite (δ) along with suppression of both austenite formation and other intermetallic precipitation [41,42].

As shown in Fig. 7, the Euler color map revealed a uniform appearing square-like mosaic macrostructure with each tessera size ranging from 60-100 μm. The resulting macrostructure formed due to the adopted laser scanning strategy during PBF-LB/M. Upon closer examination, smaller recrystallized grains ranging from 1 to 20 μm were observed near the tessera boundaries. Fig. 7(d) shows that the distribution of low and high angle grain boundaries is uneven. The higher proportion of low angle grain boundary fraction compared to high angle fraction primarily stems from the directional solidification of molten metal liquid during the PBF-LB/M process [43].

3.2. Mechanical properties

The nano hardness (H) and elastic modulus (E) of PBF/LB built NiFSS derived from the load–displacement curve (Fig. 8) of the instrumented nano-indentation was reported as 3.39 ± 0.13 GPa and 238 ± 9.0 GPa, respectively. In the previous studies, the H and E of PBF-LB/M −built 316L SS samples have been documented as 2.84 ± 0.039 GPa and 141.18 ± 2.48 GPa, respectively [32]. When the manufacturing route is PBF-LB/M, 316L steels have austenitic microstructure whereas NiFSS

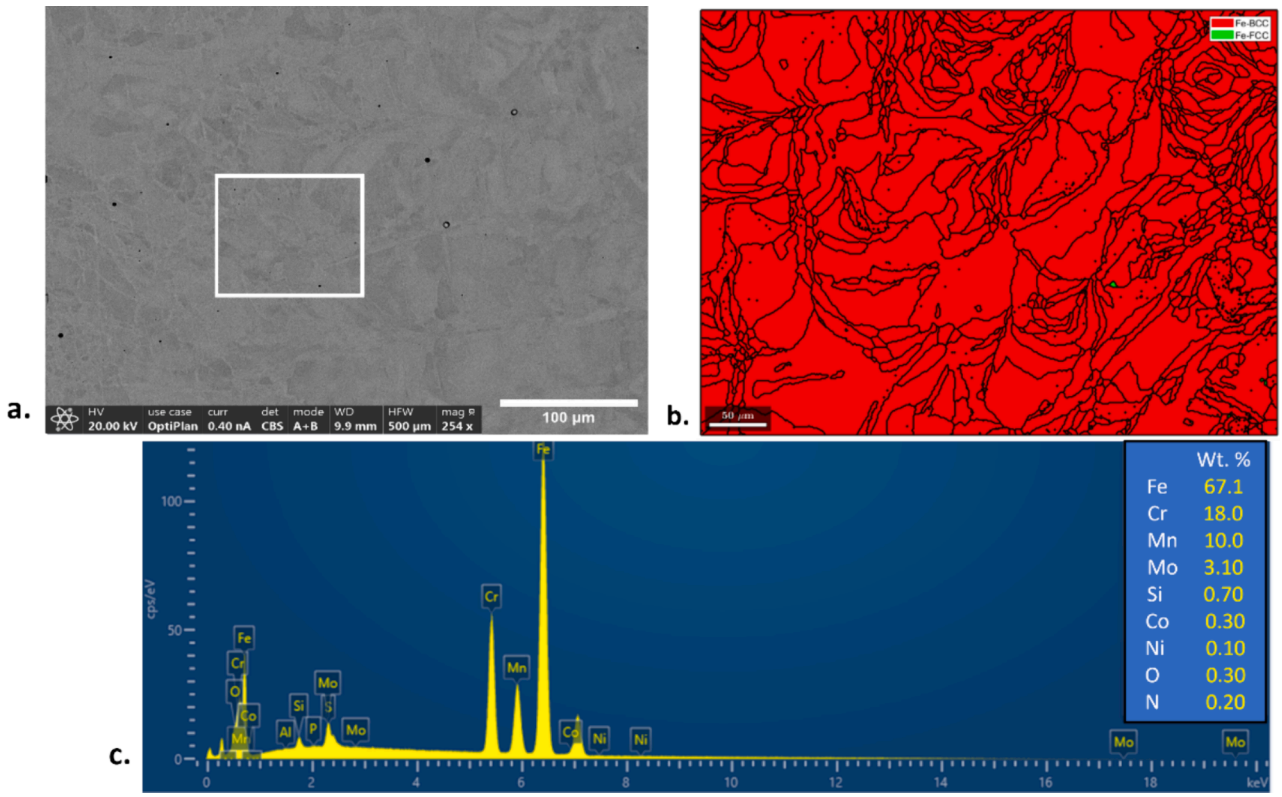

Fig. 5. (a) SEM micrographs of the as-built sample after polishing (b) EBSD phase mapping (red-BCC, green-FCC) (c) EDS for detecting elements in the scanned region (marked as rectangle region). (For interpretation of the references to color in this figure legend, the reader is referred to the web version of this article.)

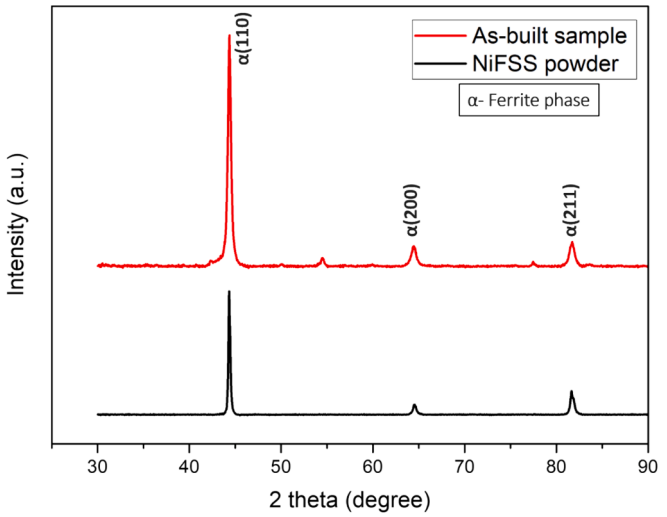

Fig. 6. XRD pattern of Ni-free stainless steel powder and PBF-LB/M −built sample.

has ferrite phase (Fig. 5) in the matrix [44]. Ferrite has been recognized as the harder phase, as confirmed by nanoindentation analyses revealing superior mechanical properties, specifically higher elastic modulus and hardness, in comparison to austenite [45].

3.3. Tribology testing

The relationship between the coefficient of friction (CoF) and the sliding time of NiFSS is illustrated in Fig. 9. In dry conditions, the average CoF for NiFSS is found (Fig. 9(c)) to be 0.17 ± 0.02 and 0.28 ± 0.01 for linear and eight/butterfly sliding configurations, respectively. Meanwhile, under SBF lubrication, the CoF decreases to 0.08 ± 0.01 and 0.15 ± 0.03 for linear and eight/butterfly sliding geometries, respectively. The CoF of PBF-LB/M −built 316L SS was reported as 0.5 in a ball on disk configuration (316L SS/Al_2O_3 sliding pairs) for linear profile under Phosphate Buffered Saline (PBS) fluid at a temperature of 37 °C [12], which is approximately 2 times higher than that of the PBF-LB/M −built NiFSS (0.17 and 0.28 for linear and eight/butterfly sliding geometry under dry condition). The decreased CoF of NiFSS is due to its superior hardness (3.39 GPa) and elastic modulus (238 GPa). In Fig. 9 (b), it is evident that the coefficient of friction (CoF) of NiFSS stabilizes under SBF lubrication approximately after 2 min of sliding, contrasting with the dry condition where the CoF fails to stabilize even after 30 min of sliding. This disparity is attributed to continuous formation of wear debris with a stick–slip behavior over time in the dry condition, resulting in a three-body abrasive wear mechanism. During the tribology test, the sliding geometry obtained was eight (a combination of two nearly circles with their centers, i.e., butterfly geometry). Due to the intricate nature of this geometry, the applied load fluctuated by approximately 5 N, which affected the coefficient of friction and, in turn, the smoothness of the curve in the CoF versus sliding time graph (depicted in Fig. 9(a) and (b)) under both dry and SBF conditions.

The wear volume (W_v) for both the linear and eight/butterfly sliding geometries is obtained from optical profilometry of wear scars, as illustrated in Fig. 10. The pseudo colors depicted in Fig. 10 indicate the depth of the wear scar, with the magenta color highlighting a greater worn depth observed in both linear and eight/butterfly sliding geometries under dry conditions. The measured wear volume from optical profilometry is used to calculate the wear rate (W_R) by using Archard's wear equation. Fig. 9(d) presents the average wear rate (W_R) of NiFSS under applied loads of 60 N and a sliding speed of 10 mm/s, comparing the results in both dry and SBF solutions for linear and eight/butterfly sliding geometries. In dry conditions, the average wear rate of NiFSS was found to be 5.70 ± 0.05 × 10^{-6} mm^3/N.m and 6.60 ± 0.03 × 10^{-6} mm^3/

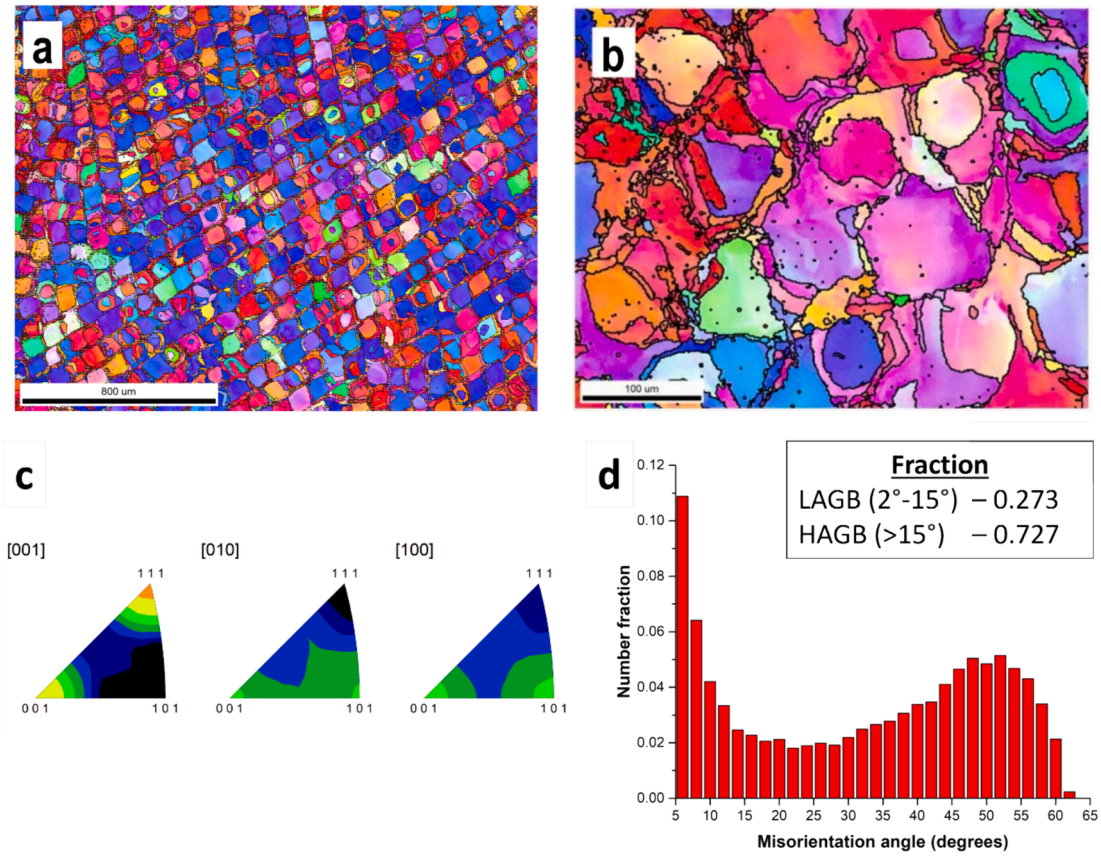

Fig. 7. (a), (b) Euler color mapping based on EBSD Data for depicting the grain morphology of as-built sample (c) Inverse pole figure (IPF) (d) Distribution of misorientation angle (low and high angle grain boundaries (LAGB, HAGB)).

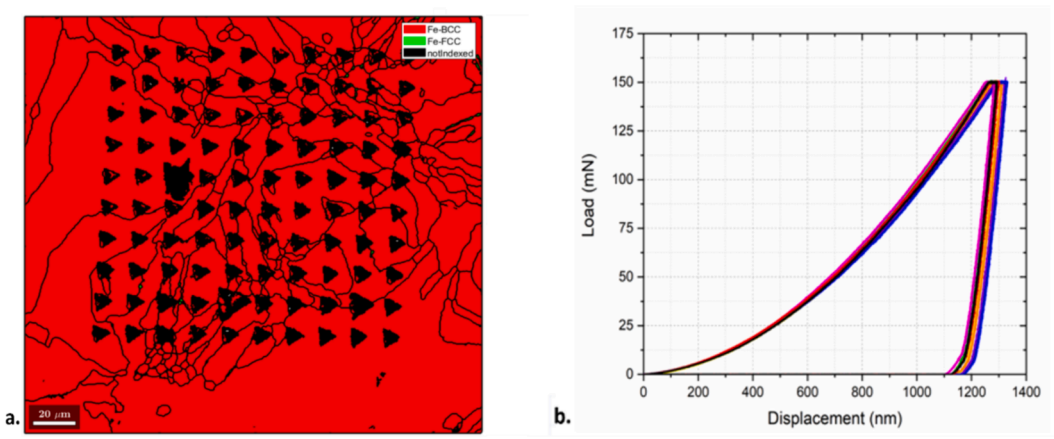

Fig. 8. (a) EBSD mapping of as-built NiFSS (b) Load displacement curve.

N.m for linear and eight/butterfly sliding geometries, respectively. Conversely, under SBF lubrication, the average wear rate decreased to $1.60 \pm 0.03 \times 10^{-6}$ mm^3/N.m and $3.10 \pm 0.06 \times 10^{-6}$ mm^3/N.m for linear and eight/butterfly sliding geometries, respectively. Moreover, a greater wear rate (33×10^{-6} mm^3/N.m) was observed for PBF-LB/M built 316L SS in a ball on disk configuration (316L SS/Al_2O_3 sliding pairs) under Phosphate Buffered Saline (PBS) fluid at a temperature of 37 °C [12]. The notable reduction in wear rate for PBF-LB/M built NiFSS compared to that of PBF-LB/M built 316L SS can be attributed to the higher hardness (H: 3.39 ± 0.13 GPa) and elastic modulus of NiFSS (E: 141.18 ± 2.48 GPa) in contrast to the 316L SS (H: 2.84 ± 0.039 3.26 GPa and E: 141.18 ± 2.48 GPa). In the dry tribology condition, the wear rate of NiFSS is roughly 3.5 and 2.1 times greater than that observed under SBF lubrication, respectively. This notable increase in wear rate in the dry environment may be attributed to the increased contact surface between the counter zirconia ball and the surface of the NiFSS and a shift in the wear mechanism from adhesive wear to two/three body abrasive wear. Additionally, it is noteworthy that the decrease in CoF for NiFSS is significant, with a reduction of approximately 53 % for linear sliding and 46 % for eight/butterfly sliding configurations when compared to their respective dry conditions (linear: 0.17, eight/butterfly: 0.28). This decline in CoF could possibly be ascribed to the formation of a protective layer of SBF on the contact surfaces of the materials. In comparison to the wear rate of linear sliding geometry, a notable increase in wear

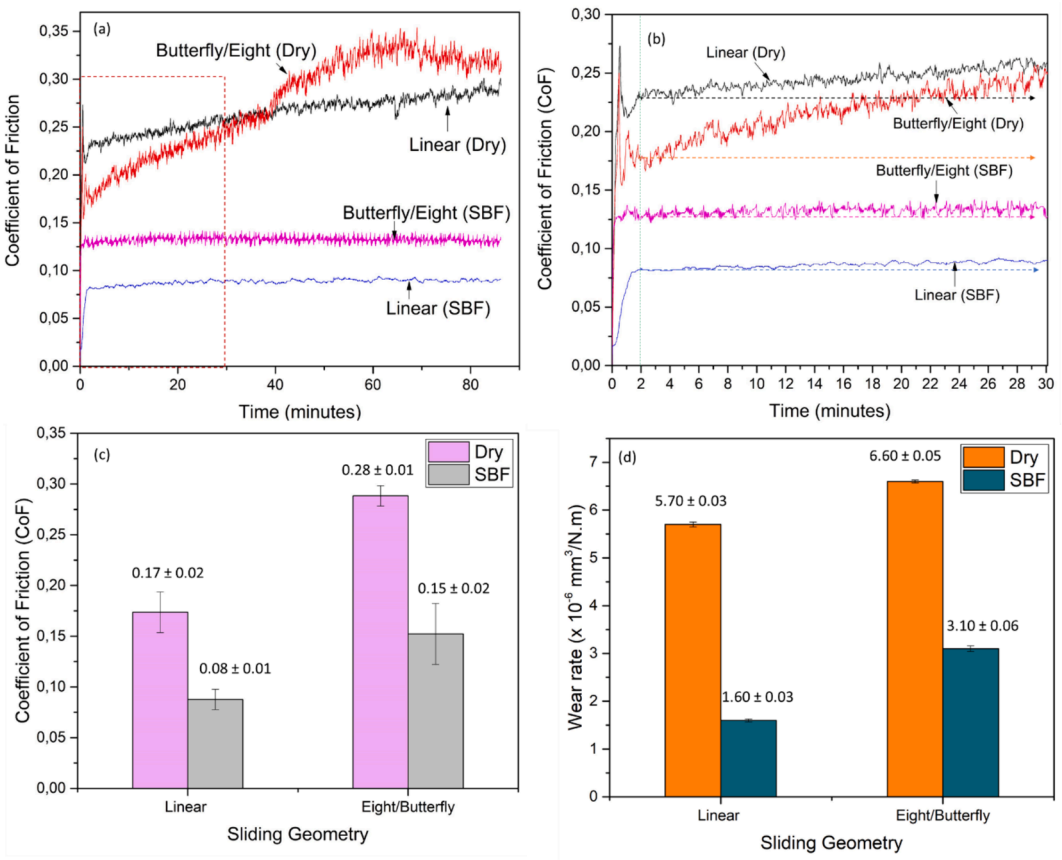

Fig. 9. (a) Plots of coefficient of friction (CoF) of PBF-LB/M built NiFSS vs. the sliding time; (b) magnified plot of the average friction coefficient vs. the sliding time to check the stabilization of CoF (c) the average CoF, and (d) average wear rate of NiFSS under dry and SBF lubrication.

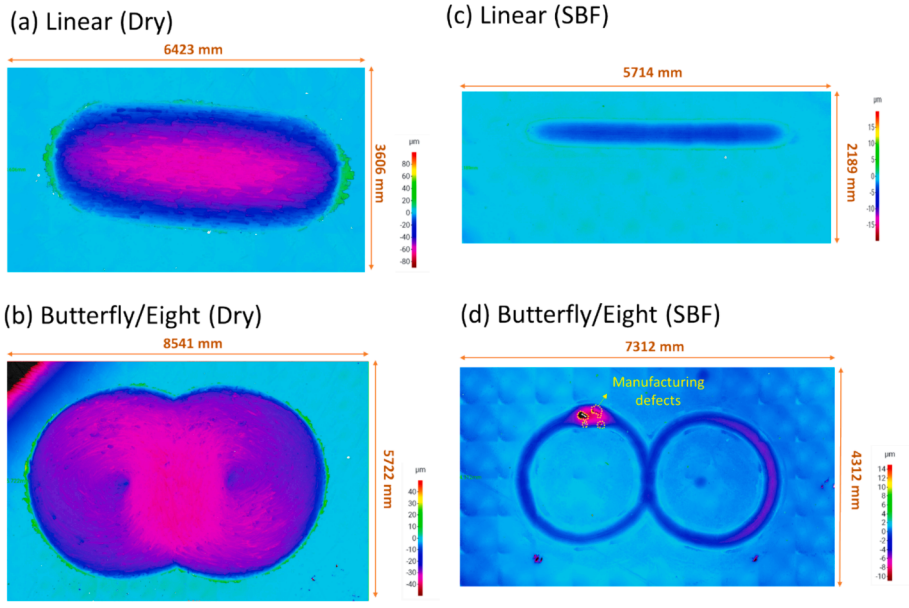

Fig. 10. Optical profilometry images showing an overview of the sliding geometries on NiFSS surface, (a-b) linear and eight/butterfly sliding geometries in dry (c-d) linear and eight/butterfly sliding geometries in SBF lubrication. Psedu colors represent the depth of wear scar.

damage was observed in the eight/butterfly sliding configuration, with wear rate showing approximately 16 % and 94 % higher values (W_R: $6.60 \pm 0.03 \times 10^{-6}$ mm^3/N.m in dry and W_R: $3.10 \pm 0.06 \times 10^{-3}$ mm^3/N.m in SBF). The complexity of sliding geometry of eight/butterfly produces two frictional forces in x and y directions which contribute to its higher friction (CoF: 0.28 ± 0.01 in Dry and CoF: 0.15 ± 0.02 in SBF) and therefore higher wear rate than that of simple linear sliding configuration [46].

The NiFSS sample exhibited the least amount of wear (W_R: $1.60 \pm 0.03 \times 10^{-6}$ mm^3/N.m) when subjected to linear sliding geometry with

SBF lubrication, and it was characterized by the lowest average coefficient of friction of 0.08 (Fig. 9(c)).

The optical micrographs of damaged surfaces are shown in Fig. 11 (a–f). The double-headed arrow shows the sliding direction on the surfaces. The optical micrographs reveal the micro morphologies of samples and show the presence of manufacturing defects on eight/butterfly sliding geometry tested under SBF lubrication (Fig. 11(d)).The wear depth profiling of NiFSS was revealed through optical profilometry of both linear and eight/butterfly sliding geometries, as depicted in Fig. 11 (e–h). In the case of dry conditions, the average wear depth of the NiFSS sample was measured as 22.5 ± 0.5 μm for linear sliding geometry and 24.5 ± 0.2 μm for eight/butterfly sliding geometry. However, under SBF lubrication, a significant reduction in wear depth was observed, with values of 1.23 ± 0.04 μm for linear sliding and 2.21 ± 0.02 μm for eight/butterfly sliding geometry. In dry condition, the NiFSS sample showed the highest wear depth (24.5 ± 0.2 μm) when subjected to eight/butterfly sliding geometry, whereas under SBF lubrication, the lowest wear depth (1.23 ± 0.04 μm) was observed for the sample in linear sliding geometry, thus confirming the enhanced wear resistance facilitated by presence SBF lubricating layer. The optical profilometer measured the average roughness (R_a) of the worn surfaces to be 0.821 ± 0.007 μm and 0.915 ± 0.009 μm for linear and eight/butterfly sliding geometries, respectively, under dry conditions. However, under SBF lubrication, the average surface roughness decreased significantly, with measurements of 0.082 ± 0.001 μm and 0.126 ± 0.002 μm for linear and eight/butterfly sliding geometries, respectively. The notable decrease in surface roughness by 90 % and 86 % for linear and eight/butterfly sliding geometries, respectively, under SBF lubrication compared to their counterparts under dry conditions (with R_a values of 0.082 μm for linear and 0.126 μm for eight/butterfly) complementing with the lower CoF observed such as 0.08 and 0.15 for linear and eight/butterfly sliding geometries, respectively. Moreover, the elevated surface roughness and wear depth observed in the eight/butterfly sliding configuration, under both dry and SBF conditions, correspond to its higher wear depth, wear rate, and CoF values compared to the linear sliding geometry.

The SEM micrographs, presented in Fig. 12(a), demonstrate the abrasive wear and delamination as a dominant wear mechanism in NiFSS. In the dry condition, more pronounced abrasive grooves are observed in both linear and eight/butterfly sliding geometries, whereas smoother abrasive grooves are evident for these sliding configurations under SBF lubrication (Fig. 12(d,e,f)). Under dry conditions, the cracks are discernible on the sliding path (Fig. 12(i)). Additionally, the displaced material has been dissected due to hard asperities, resulting in local fractures and cracks around the grooves. The cyclic loading causes fatigue and delamination wear for both linear and eight/butterfly sliding geometry under dry conditions (Fig. 12(k–l)). Displacement of materials in abrasive grooves due to the connection between cyclic cracks provides evidence of the poor strength of NiFSS under dry conditions. Under SBF lubrication, the NiFSS sample shows an undamaged surface with smoother abrasive grooves (Fig. 12(h)). The smoother abrasive grooves are observed in both linear and eight/butterfly sliding geometry, providing evidence of resistance of SBF lubrication to crack formation around the grooves. Furthermore, under dry loading conditions, the wear particles removed from the NiFSS surface may activate other wear mechanisms (third body mechanism), and therefore, the wear rate of NiFSS under dry condition is significantly increased compared to the wear rate of the NiFSS under SBF lubrication. The increased wear rate values (Fig. 9d), nearly 53 % for linear sliding (5.70 ± 0.05 × 10^{-6} mm^3/N.m) and 46 % for eight/butterfly sliding configuration (6.60 ± 0.03 × 10^{-6} mm^3/N.m) under dry conditions, clearly indicate a significant contrast with their counterparts under SBF lubrication. Additionally, the wear depth analysis (Fig. 11(e–h)) revealed a notable decrease in the depth of wear grooves on the surface of the NiFSS under SBF lubrication, indicating the lubricating influence of SBF. Specifically, under SBF lubrication, significant reductions that are in wear depth were observed, with measurements of 1.23 ± 0.04 μm for linear sliding (22.5 ± 0.5 μm under dry) and 2.21 ± 0.02 μm for eight/butterfly sliding geometry (24.5 ± 0.2 μm under dry). In the supplementary data (Fig. S2), the EDS elemental mapping of the linear sliding geometry under SBF condition reveals the composition of NiFSS and a significant presence of oxygen within the worn track and its edge, as indicated by spectra 2, 3, and 4. This increased oxygen content is likely attributed to the increased surface area exposure to atmosphere and the presence of SBF. Also, with complex sliding geometry that is eight/butterfly, the depth of grooves created by abrasive particles on the worn surface increased compared to simple linear sliding geometry. The complex sliding geometry experiences higher frictional force in both x and y directions; thus, there is a significant variation in the wear rate concerning the sliding geometry. With linear sliding geometry, the cutting and grooving types of wear take place, and the subsurface deformation is negligible; however, with complex eight/butterfly geometry, the micro-cracks near abrasive grooves cause substantial delamination and wear.

In summary, the discussion outlined above is visually represented in Fig. 13, illustrating the relationship between wear and sliding configurations (linear and eight/butterfly) under different experimental conditions (dry and SBF). As depicted in Fig. 13, the PBF-LB/M built NiFSS with linear sliding geometry under SBF lubrication exhibits minimal cracks and smooth abrasive grooves at the interface of the ZrO_2 ball and NiFSS, indicating the highest wear resistance with a CoF of 0.08, wear rate of 1.60 × 10^{-6} mm^3/N.m, and wear depth of 1.23 μm among all experimental conditions. Conversely, a noticeable number of cracks, deeper abrasive grooves, and delaminations are observed in the case of eight/butterfly sliding geometry under dry conditions, indicative of its lowest damage tolerance behavior with a CoF of 0.28, wear depth of 24.5 μm, and wear rate of 6.60 × 10^{-6} mm^3/N.m. This can be likely be attributed to the intricate nature of the eight geometries, which comprises two nearly circular shapes with two distinct centers. This complex geometry poses challenges for the bio-tribometer to uniformly apply the normal load, resulting in a variation of approximately ± 5 N, consequently impacting the coefficient of friction (CoF) (Fig. 9(a,b)). During the tribology experiment, when a normal load (F) is applied onto the PBF-LB/M built NiFSS sample, the linear sliding configuration experiences only one frictional force (f) in the ± x direction. In contrast, the eight/butterfly sliding geometry encounters two frictional forces, namely f_t in the ± x direction and fc in the ± y directions. Additionally, there is a change in the direction (by 180°) of the centripetal force (f_c) at the junction of the two circles. Consequently, the resultant frictional force (f_{net}) in the eight/butterfly sliding geometry is higher than the frictional force (f) observed in the linear sliding geometry. Therefore, The CoF, wear depth, and wear rate of the eight/butterfly geometry are significantly higher than those of the linear configuration.

3.4. Biocompatibility of NiFSS

The biocompatibility assay demonstrated a steady, exponential increase in cell numbers from the beginning of the experiment until day 10 in control wells (Fig. 14(a)), indicating normal proliferation and viability of MC3T3-E1 cells. However, when cells were grown on top of NiFFS or 316L SS samples, cell numbers remained lower throughout the experiment. On day 10, the cell number in control wells was significantly higher when compared to NiFSS ($p \leq 0.001$) or 316L SS ($p \leq 0.001$). There was no significant difference in cell numbers between the NiFSS and 316L SS groups, but the cells seemed to grow slightly better on top of NiFSS than 316L SS. Microscopic images verified that the cells were viable when cultured in the presence of NiFSS or 316L SS (Fig. 14 (b)), indicating no severe cytotoxicity.

The material topography, such as surface roughness, is known to affect cell viability and adhesion [47]. In our experiments, cells were cultured both on standard polystyrene cell culture plastic and on polished metal pieces, which can explain the differences observed between control and stainless steel groups. It is also important to note that besides

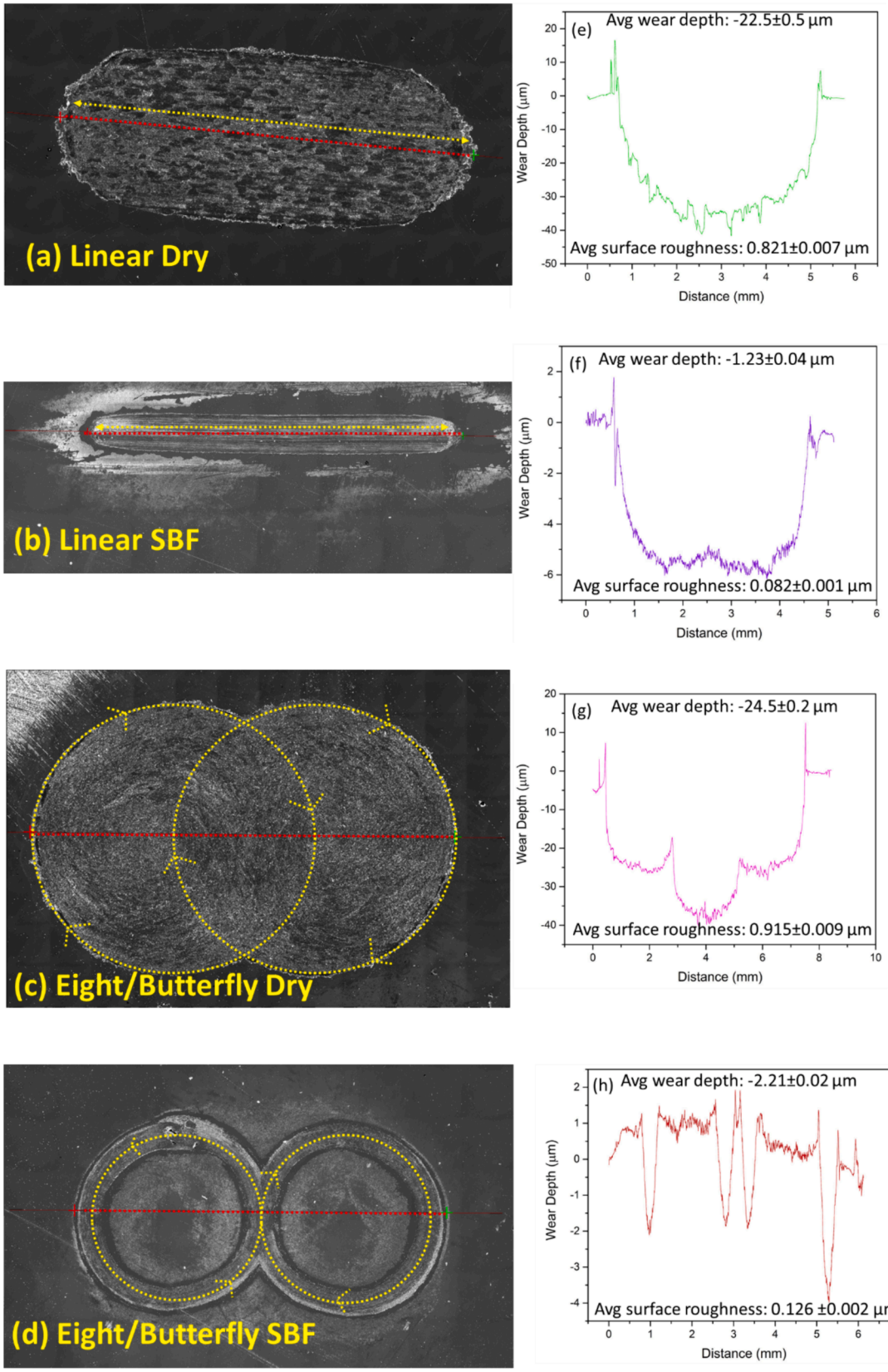

Fig. 11. (a-d) Optical micrographs showing an overview of the sliding geometries on NiFSS surface, (e-h) wear scars against ZrO_2 ball at 60 N load of NiFSS imaged using optical profilometry. The double-headed arrow indicates the sliding path.

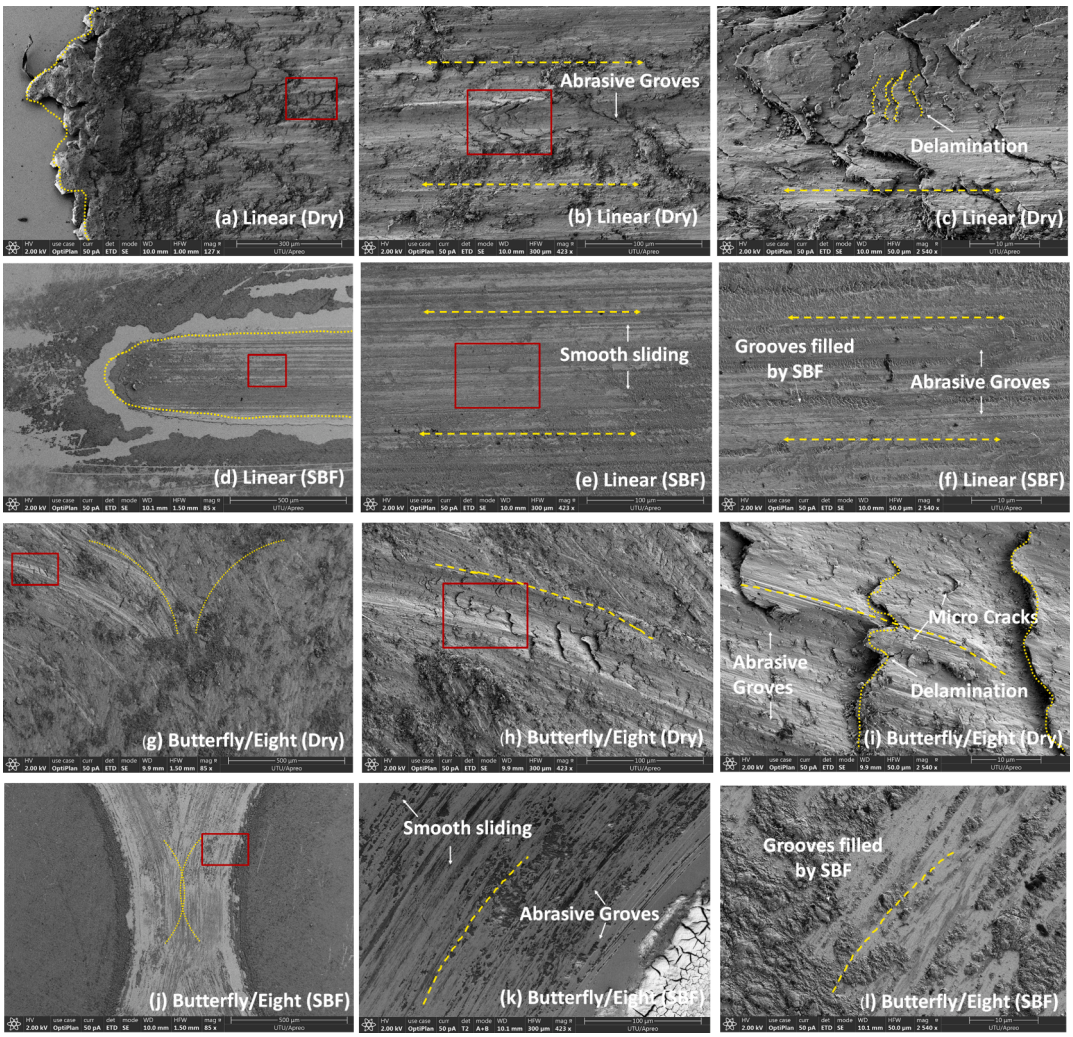

Fig. 12. Scanning electron micrographs of linear (a-c) under dry (d-f) under SBF and eight/butterfly (g-i) under dry (j-l) under SBF at various magnifications.

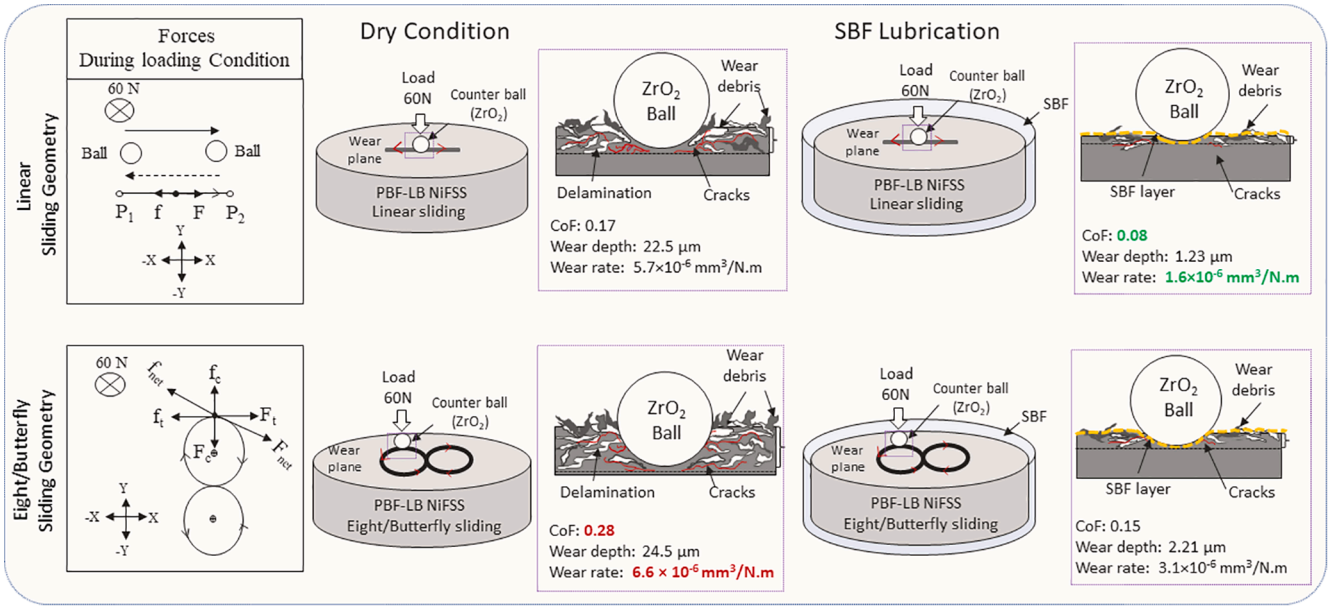

Fig. 13. Schematic of the effect of various sliding geometries on wear on the surface of PBF-LB/M built NiFSS in dry conditions and SBF lubrication (conditions: normal load: 60 N, against ZrO_2 ball).

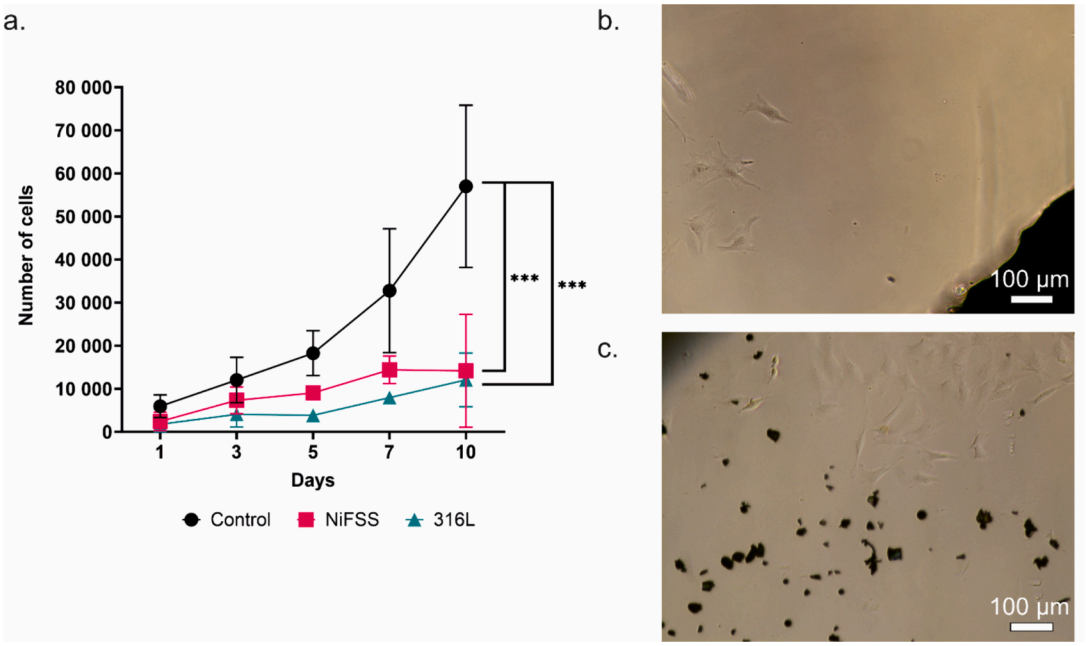

Fig. 14. The number of viable cells cultured on normal cell culture plastic (control) or on top of NiFSS or 316L stainless steel (a). Representative light microscopic images taken with 20X magnification of cells growing on cell culture plastic surface next to a piece of 316L SS on day 5 of culture (b) and near NiFSS debris (c) on day 7 of culture. Statistical significance is referred to as ***$p \leq 0.001$.

the optimal surface for cell adhesion, the cells in the control group had more surface area to grow on, which can also contribute to better viability. In addition, wear particles of metallic implant materials are known to cause cell toxicity [48] and in the NiFSS group, particle debris were observed (Fig. 14(c)), which were accumulating over time in culture. Such debris could originate from NiFSS due to the manufacturing process. Since no similar debris were seen in the control wells, this could indicate that the debris originating from stainless steel materials can further negatively affect cell viability.

It should be furthermore noted that there was significant inter-experimental variation between the cytotoxicity repeats. It is well-known that biological assays are prone to high variation, but part of such a high variation might also be due to the reuse of samples from the first two repeats in the third and fourth repeat. Even though the pieces were carefully cleaned and re-sterilized, some debris might still have adhered to the metal surface, which could further affect cell growth.

However, besides the chemical composition and particle size of the material, cell viability in vivo depends also on the consequent changes in the osteoimmunological microenvironment, where the initial stages of bone healing processes are regulated by macrophages. It is possible that the NiFSS debris seen in Fig. 14(c) could promote crosstalk between the immune system and bone cells and lead to wear particle induced chronic inflammation and promote osteoclast activation and fibrous encapsulation of the materials. On the other hand, if the acute inflammation after debris clearance of NiFSS can be resolved without leading to chronic inflammation it may promote bone regeneration via progenitor cell recruitment, which will be a matter of future studies.

4. Conclusions

The optimized process parameters (laser power 160 W, scanning speed 600 mm/sec, hatch distance 0.08 mm and layer thickness 0.03 mm) for PBF-LB/M of NiFSS yielded samples with relative density of 98.469 %. In the as-built state, NiFSS samples exhibited fully ferritic phase in the microstructure. The PBF-LB/M built NiFSS exhibits a lower CoF value and wear rate compared to PBF-LB/M –built 316LSS, indicating its potential for improved tribological performance attributed by its superior hardness and elastic modulus. The wear volume and rate of NiFSS are significantly lower under SBF lubrication compared to dry conditions, highlighting the effectiveness of lubrication in reducing wear. Eight/butterfly sliding geometry demonstrates higher CoF and wear rate than linear sliding geometry due to its complex nature, contributing to increased frictional forces. SEM analysis reveals abrasive wear and delamination as dominant wear mechanisms in NiFSS, with reduced damage observed under SBF lubrication. The wear depth analysis shows a significant decrease in wear depth under SBF lubrication, indicating the lubricating effect of SBF and reduced damage to the surface. There were no significant differences in osteoblast-like cell viability between the NiFSS and 316L SS samples, but the cells seemed to grow slightly better on top of NiFSS than 316L SS during the culture period of 10 days. In summary, this study underscores the significance of optimizing process parameters for PBF-LB/M fabrication of NiFSS, highlighting its promising mechanical properties, superior tribological performance, and potential for biomedical applications, thereby contributing to advancements in additive manufacturing and material science.

Author contributions

Chinmayee Nayak and Abhinav Anand conceptualized and conducted the experiments, analyzed the data, and contributed to writing the paper. Rahul Cherukuri conducted nanoindentation and EBSD experiments under the supervision of Gaurav Mohanty and contributed to the mechanical properties section. Karoliina Kajander and Vilma Tupala planned and conducted the cell culture experiments, analyzed the data and drafted the biocompatibility section under the supervision of Terhi J. Heino, who also secured funding for this part. Nikhil Kamboj reviewed the paper, contributed to the introduction, and the discussion on the biocompatibility section. Antti Salminen reviewed the paper, arranged the resources and secured funding. Jan Čapek, Sneha Goel and Efthymios Polatidis initiated the idea of NiFSS and subsequently assisted in PBF-LB/M NiFSS initial parameter screening, optimization and printing. Tuomas Kantonen did the printing of NiFSS. Ashish Ganvir conceived the idea, provided guidance in planning the experiments, organizing and editing the paper, and secured resources and funding for the research.

CRediT authorship contribution statement

Chinmayee Nayak: Writing – review & editing, Writing – original draft, Methodology, Investigation, Formal analysis, Data curation, Conceptualization. **Abhinav Anand:** Writing – original draft, Methodology, Investigation, Formal analysis, Data curation, Conceptualization. **Nikhil Kamboj:** Writing – review & editing, Writing – original draft. **Tuomas Kantonen:** Methodology, Investigation. **Karoliina Kajander:** Writing – original draft, Methodology, Investigation, Formal analysis, Data curation. **Vilma Tupala:** Methodology, Investigation, Formal analysis, Data curation. **Terhi J. Heino:** Writing – review & editing, Supervision, Funding acquisition. **Rahul Cherukuri:** Writing – original draft, Formal analysis, Data curation. **Gaurav Mohanty:** Writing – review & editing, Supervision. **Jan Čapek:** . **Efthymios Polatidis:** Writing – review & editing, Supervision, Resources, Conceptualization. **Sneha Goel:** Methodology, Conceptualization. **Antti Salminen:** Writing – review & editing, Resources, Funding acquisition. **Ashish Ganvir:** Writing – review & editing, Supervision, Resources, Funding acquisition, Conceptualization.

Declaration of competing interest

The authors declare that they have no known competing financial interests or personal relationships that could have appeared to influence the work reported in this paper.

Data availability

Data will be made available on request.

Acknowledgements

Ermei Mäkilä for performing the Scanning Electron Microscope and X-ray Diffraction, Inka.W. Vaisanen and Eter.S. Tourunen for performing the optical profilometry, Aki Piiroinen for Assisting with Tribology Laboratory at DMS, UTU. Frej Bjondahl for performing particle size distribution. Funding: DREAMS TEKN TOT (2600577911); Tenure-track grant to Prof. Ganvir by UTU. Department of Mechanical and Materials Engineering for funding the MSc thesis of Mr. Tuomas Kantonen. Adjunct Prof. Terhi J. Heino holds Business Finland Co-innovation Grant number 11/31/2023.

Appendix A. Supplementary data

Supplementary data to this article can be found online at https://doi.org/10.1016/j.matdes.2024.113013.

References

[1] K. Yang, Y. Ren, Nickel-free austenitic stainless steels for medical applications, Sci. Technol. Adv. Mater. 11 (2010) 014105, https://doi.org/10.1088/1468-6996/11/1/014105.
[2] Uggowitzer Ruth Magdowski, M.O. Speidel, Nickel Free High Nitrogen Austenitic Steels, ISIJ International, 36 (1996). https://doi.org/10.2355/isijinternational.36.901.
[3] L. Patnaik, S.R. Maity, S. Kumar, Status of nickel free stainless steel in biomedical field: A review of last 10 years and what else can be done 7 (2019) 638–643, https://doi.org/10.1016/j.matpr.2019.12.205.
[4] U.I. Thomann, P.J. Uggowitzer, Wear-corrosion behavior of biocompatible austenitic stainless steels, 239 (2000), Pages 48-58, https://doi.org/10.1016/S0043-1648(99)00372-5.
[5] IARC Working Group, on the Evaluation of Carcinogenic Risks to Humans., International Agency for Research on Cancer., Chromium, nickel and welding, IARC 49 (1990).
[6] P.J. Uggowitzer, W.F. Bähre, H. Wohlfromm, M.O. Speidel, Nickel-free high nitrogen austenitic stainless steels produced by metal injection moulding, Mater. Sci. Forum 318 (1999) 663–672, https://doi.org/10.4028/www.scientific.net/msf.318-320.663.
[7] M. Fini, N.N. Aldini, P. Torricelli, G. Giavaresi, V. Borsari, H. Lenger, J. Bernauer, R. Giardino, R. Chiesa, A. Cigada, A new austenitic stainless steel with negligible nickel content: An in vitro and in vivo comparative investigation, Biomaterials 24 (2003) 4929–4939, https://doi.org/10.1016/S0142-9612(03)00416-2.
[8] G. Stein, I. Hucklenbroich, Manufacturing and applications of high nitrogen steels, Mater. Manuf. Process. 19 (2004) 7–17, https://doi.org/10.1081/AMP-120027494.
[9] A. Jadhav, V.S. Jadhav, A review on 3D printing: an additive manufacturing technology, Mater. Today:. Proc. 62 (2022) 2094–2099, https://doi.org/10.1016/j.matpr.2022.02.558.
[10] M.H. Mobarak, M.A. Islam, N. Hossain, M.Z. Al Mahmud, M.T. Rayhan, N.J. Nishi, M.A. Chowdhury, Recent advances of additive manufacturing in implant fabrication – A review, Appl. Surf. Sci. Advances 18 (2023), https://doi.org/10.1016/j.apsadv.2023.100462.
[11] M. Vignesh, G. Ranjith Kumar, M. Sathishkumar, M. Manikandan, G. Rajyalakshmi, R. Ramanujam, N. Arivazhagan, Development of biomedical implants through additive manufacturing: a review, J. Mater. Eng. Perform. 30 (2021) 4735–4744, https://doi.org/10.1007/s11665-021-05578-7.
[12] F. Bartolomeu, M. Buciumeanu, E. Pinto, N. Alves, O. Carvalho, F.S. Silva, G. Miranda, 316L stainless steel mechanical and tribological behavior—A comparison between selective laser melting, hot pressing and conventional casting, Addit. Manuf. 16 (2017) 81–89, https://doi.org/10.1016/j.addma.2017.05.007.
[13] J. Stendal, O. Fergani, H. Yamaguchi, N. Espallargas, A comparative tribocorrosion study of additive manufactured and wrought 316L stainless steel in simulated body fluids, J. Bio. Tribocorros. 4 (2018), https://doi.org/10.1007/s40735-017-0125-9.
[14] A. Brończyk, P. Kowalewski, M. Samoraj, Tribocorrosion behaviour of Ti6Al4V and AISI 316L in simulated normal and inflammatory conditions, Wear 434–435 (2019), https://doi.org/10.1016/j.wear.2019.202966.
[15] Q. Liu, J. Lu, Z. Luo, J. Yi, M. He, Y. Zhao, S. Wang, Enhancing corrosion resistance of additively manufactured 316L stainless steel by fabricating pillar arrays, Mater. Des. 230 (2023), https://doi.org/10.1016/j.matdes.2023.111940.
[16] M.H. Shaeri Karimi, M. Yeganeh, S.R. Alavi Zaree, M. Eskandari, Corrosion behavior of 316L stainless steel manufactured by laser powder bed fusion (L-PBF) in an alkaline solution, Opt Laser Technol 138 (2021). https://doi.org/10.1016/j.optlastec.2021.106918.
[17] S.M.J. Moghadas, M. Yeganeh, S.R.A. Zaree, M. Eskandari, Influence of low temperature heat treatment on microstructure, corrosion resistance and biological performance of 316L stainless steel manufactured by selective laser melting, CIRP J. Manuf. Sci. Technol. 40 (2023) 68–74, https://doi.org/10.1016/j.cirpj.2022.11.006.
[18] G.A. Kantonen Tuomas, Producing novel stainless steels by laser powder bed fusion additive manufacturing, https://www.utupub.fi/bitstream/handle/10024/174714/Kantonen_Tuomas_Thesis.pdf?sequence=1 (accessed January 6, 2024).
[19] L. Liu, T. Minasyan, N. Kamboj, S. Aydinyan, I. Hussainova, Bio-inspired TiB2-TiB-TiN lattices by selective laser melting, Mater. Lett. 277 (2020) 128337, https://doi.org/10.1016/j.matlet.2020.128337.
[20] N. Kamboj, A. Ressler, I. Hussainova, Bioactive ceramic scaffolds for bone tissue engineering by powder bed selective laser processing: A review, Mater. 14 (2021), https://doi.org/10.3390/ma14185338.
[21] M. Yeganeh, Z. Shahryari, A. Talib Khanjar, Z. Hajizadeh, F. Shabani, Inclusions and Segregations in the Selective Laser-Melted Alloys, A Review, Coatings 13 (2023), https://doi.org/10.3390/coatings13071295.
[22] C. Nayak, P. Singh, K. Balani, Contact stress and sliding wear damage tolerance of hydroxyapatite and carbon nanotube reinforced polyethylene cup liner against zirconia femoral head, J. Mech. Behav. Biomed. Mater. 136 (2022), https://doi.org/10.1016/j.jmbbm.2022.105435.
[23] C. Nayak, P. Kushram, M.A.A. Zaidi, I. Singh, J. Sen, K. Balani, Multi-length scale strengthening and cytocompatibility of ultra high molecular weight polyethylene bio-composites by functionalized carbon nanotube and hydroxyapatite reinforcement, J. Mech. Behav. Biomed. Mater. 140 (2023), https://doi.org/10.1016/j.jmbbm.2023.105694.
[24] H.C. Zhao, Y. Bin Ren, J.H. Dong, X.M. Fan, K. Yang, Effect of cold deformation on the friction-wear property of a biomedical nickel-free high-nitrogen stainless steel, Acta Metallurgica Sinica (English Letters) 29 (2016) 217–227, https://doi.org/10.1007/s40195-016-0388-z.
[25] C. Birleanu, M. Pustan, G. Pop, M. Cioaza, F. Popa, L. Lazarescu, G. Contiu, Experimental investigation of the tribological behaviors of carbon fiber reinforced polymer composites under boundary lubrication, Polymers 14 (2022), https://doi.org/10.3390/polym14183716.
[26] P.L. Menezes, S.V. Kishore, Kailas, Influence of surface texture on coefficient of friction and transfer layer formation during sliding of pure magnesium pin on 080 M40 (EN8) steel plate, Wear 261 (2006) 578–591, https://doi.org/10.1016/j.wear.2006.01.001.
[27] Y. Reneta Nafu, W. Kingsly Mofor, The effect of speed on coefficient of friction in african plum oil (Dacryodes Edulis)Lubricant, Asian Journal of Engineering and Technology 10 (2022), https://doi.org/10.24203/ajet.v10i4.7054.
[28] Wyman Street, Waltham, 4 - Friction–vibration interactions, in: Handbook of Friction-Vibration Interactions. MA 02451,USA, Woodhead Publishing, 2014, pp. 153–305, https://doi.org/10.1533/9780857094599.153.
[29] Y. Ren, K. Yang, B. Zhang, In vitro study of platelet adhesion on medical nickel-free stainless steel surface, Mater. Lett. 59 (2005) 1785–1789, https://doi.org/10.1016/j.matlet.2005.01.067.
[30] D. Gianoglio, N. Ciftci, S. Armstrong, V. Uhlenwinkel, L. Battezzati, On the cooling rate-microstructure relationship in molten metal gas atomization, Metall. Mater. Trans. A 52 (2021) 3750–3758, https://doi.org/10.1007/s11661-021-06325-2.
[31] W.T. DeLong, A modified phase diagram for stainless steel weld metals, Metal Progress 77 (1960) 99–100B.

[32] C. Cui, V. Uhlenwinkel, A. Schulz, H.W. Zoch, Austenitic stainless steel powders with increased nitrogen content for laser additive manufacturing, Metals (basel) 10 (2020), https://doi.org/10.3390/met10010061.
[33] F. Bachmann, R. Hielscher, H. Schaeben, Grain detection from 2d and 3d EBSD data—Specification of the MTEX algorithm, Ultramicroscopy 111 (2011) 1720–1733, https://doi.org/10.1016/j.ultramic.2011.08.002.
[34] P. Sudharshan Phani, W.C. Oliver, A critical assessment of the effect of indentation spacing on the measurement of hardness and modulus using instrumented indentation testing, Mater Des 164 (2019), https://doi.org/10.1016/j.matdes.2018.107563.
[35] W.C. Oliver, G.M. Pharr, Nanoindentation in materials research: Past, present, and future, MRS Bull. 35 (2010) 897–907, https://doi.org/10.1557/mrs2010.717.
[36] W.C. Oliver, G.M. Pharr, Measurement of hardness and elastic modulus by instrumented indentation: Advances in understanding and refinements to methodology, 2004. www.mrs.org/publications/jmr/policy.html.
[37] T. Kokubo, H. Takadama, How useful is SBF in predicting in vivo bone bioactivity? Biomaterials 27 (2006) 2907–2915, https://doi.org/10.1016/j.biomaterials.2006.01.017.
[38] A.G. Evans, Wear mechanisms in ceramics, Fundamentals Friction and Wear of Materials (1981).
[39] J.F. Archard, Contact and rubbing of flat surfaces, J. Appl. Phys. 24 (1953) 981–988, https://doi.org/10.1063/1.1721448.
[40] J. Liu, P. Wen, Metal vaporization and its influence during laser powder bed fusion process, Mater. Des. 215 (2022), https://doi.org/10.1016/j.matdes.2022.110505.
[41] H. Xiang, W. Zhao, Y. Lu, Effect of solution temperature on microstructure and mechanical properties of selective laser melted Fe-22Cr-5Ni-0.26N duplex stainless steel, Journal of Materials Research and Technology 19 (2022) 1379–1389, https://doi.org/10.1016/j.jmrt.2022.05.124.
[42] D. Kim, I. Ferretto, J.B. Jeon, C. Leinenbach, W. Lee, Formation of metastable bcc-δ phase and its transformation to fcc-γ in laser powder bed fusion of Fe–Mn–Si shape memory alloy, J. Mater. Res. Technol. 14 (2021) 2782–2788, https://doi.org/10.1016/j.jmrt.2021.08.119.
[43] F.C. Pinto, L.S. Aota, I.R. Souza Filho, D. Raabe, H.R.Z. Sandim, Recrystallization in non-conventional microstructures of 316L stainless steel produced via laser powder-bed fusion: effect of particle coarsening kinetics, J. Mater. Sci. 57 (2022) 9576–9598, https://doi.org/10.1007/s10853-021-06859-1.
[44] Z. Pitrmuc, J. Šimota, L. Beránek, P. Mikeš, V. Andronov, J. Sommer, F. Holešovský, Mechanical and microstructural anisotropy of laser powder bed fusion 316L stainless steel, Materials 15 (2022), https://doi.org/10.3390/ma15020551.
[45] K.R. Gadelrab, G. Li, M. Chiesa, T. Souier, Local characterization of austenite and ferrite phases in duplex stainless steel using MFM and nanoindentation, J. Mater. Res. 27 (2012) 1573–1579, https://doi.org/10.1557/jmr.2012.99.
[46] C. Nayak, R. Kundu, R. Pandey, K. Balani, Tribological properties of SS 304 and Ti6Al4V using four reciprocating geometries, Nanomaterials and Energy 10 (2021) 79–90, https://doi.org/10.1680/jnaen.20.00051.
[47] P. Majumdar, Cell Viability and Growth on Metallic Surfaces: in vitro Studies, Trends in Biomaterials and Artificial Organs 20 (2006) 84–89. http://www.sbaoi.org.
[48] N.A. Athanasou, The pathobiology and pathology of aseptic implant failure, Bone Joint Res 5 (2016) 162–168, https://doi.org/10.1302/2046-3758.55.BJR-2016-0086.